

High-velocity regions in planetary nebulae^{*}

Krzysztof Gesicki¹† and Albert A. Zijlstra²‡

¹ *Centrum Astronomii UMK, ul. Gagarina 11, PL-87-100 Torun, Poland.*

² *UMIST, Department of Physics, P.O. Box 88, Manchester M60 1QD, UK.*

11 November 2018

ABSTRACT

The internal velocity fields of planetary nebulae are studied with a resolution of 5 km s^{-1} . We analyze deep echelle spectra from three nebulae in the Bulge, the Sagittarius Dwarf and the SMC. No effects of metallicity is seen, except possibly a slower onset of the fast wind from the central star. Robust evidence is found for the existence of a high-velocity shock at the inner edges of the nebulae. Such a shock is predicted in hydrodynamical models but had not previously been observed. The shock gas is accelerated by the fast wind from the central star. A similar shock at the outer edges traces the expansion of the ionized shell into the ambient AGB wind. Evidence for localized regions of high velocity is also found from lines of intermediate excitation, for two of nebulae. We explore several possible interpretations: (1) an embedded shock at intermediate radii, as predicted by hydrodynamic models at the position of the outer edge of the swept-up inner shell; (2) deviations from spherical symmetry, where in some directions the intermediate-excitation lines extend into the region of the outer shock; (3) An intermediate swept-up shell, as seen in some Galactic planetary nebulae. The remaining nebula, with a [WC] star, shows strong turbulence. This may trace a superposition of many embedded shock-lets. We suggest a relation to the time-variable [WC] wind, giving a planetary nebula subjected to a multitude of sound waves.

Key words: planetary nebulae: general – planetary nebulae: individual: M 2-31, SMP 5, Wray 16-423

1 INTRODUCTION

The evolution of planetary nebulae (PNe) is driven by several distinct processes. The original density and velocity distribution are determined by the AGB mass loss. Subsequently, this is modified by the photo-ionization, and the interaction with the hot, fast wind from the central star. Together, these give rise to the intricate structures seen in many PNe.

The first models are appearing which use all of these processes to calculate the instantaneous density and velocity structure (e.g. Corradi et al. 2000a). The density structures can be obtained from high-resolution imaging, but determining the dynamical structures requires high-resolution spectra. We have developed a technique to deconvolve the velocity field from the emission line profiles. Using [O III]

and [N II], this has shown that the velocity tends to increase sharply towards the outer edge of the nebula, in agreement with hydrodynamical models. For PNe with [WC] central stars, the lines show evidence for turbulent velocity fields (Acker et al. 2002).

If a larger set of lines is available, the velocity field can be obtained with much finer radial resolution, especially if narrow-band images are also available. Such data is needed for comparison with the details of the hydrodynamic models, and in this way can test the evolution of PN nuclei and their mass loss history. Here we apply the ‘Torun models’ to deep echelle spectra of three PNe, located in the Galactic Bulge, the Sagittarius Dwarf Spheroidal galaxy and the Small Magellanic Cloud (SMC). The new data allow us to deduce the velocity fields with unprecedented detail. There are two main reasons for this improvement: lines of many ionization stages are available, and the spectral resolution of 60 000 is well fitted to the thermal broadening.

In the next sections, after a summary of the Torun models, we present the results for three objects. Evidence for several shock-like features is found. Although the objects

^{*} Based on observations obtained at the European Southern Observatory.

† email: Krzysztof.Gesicki@astri.uni.torun.pl

‡ email: a.zijlstra@umist.ac.uk

were selected based on their different metallicity, they are remarkably similar. The core masses are calculated using the dynamical age: they are all close to $0.62 M_{\odot}$. We discuss the various shocks and interpret these in terms of structures seen in the hydrodynamical models. One object shows evidence for strong turbulence: we discuss the relation between this and the shocks seen in the other nebulae.

2 OBSERVATIONS

We selected three PNe from different stellar populations: the Bulge, the Sagittarius Dwarf Spheroidal galaxy and the SMC. These have the advantage that the distances are approximately known, which benefits the photo-ionization modeling. Diameters are known from published monochromatic images for all three nebulae. One of our interests was the effect of metallicity: values for the metallicity have been published for these PNe, ranging from slightly subsolar (Bulge PN) to -0.6 dex (SMC PN). All three central stars are hot with very similar luminosity.

The observations were carried out at the ESO 3.5m NTT telescope, in August 1999. We used the echelle mode in the red arm, using grating #14 and cross disperser #3. The slit-width was $1''$ and slit length $3''$. The spectra cover the wavelength range $4300\text{--}7000\text{\AA}$ at a resolution of $R = 6 \times 10^4$, corresponding to 5 km s^{-1} : this is about the thermal line width for oxygen. The spectra were summed along the slit, flat-fielded and corrected for the response curves, using the MIDAS echelle reduction package. Each source was observed for 3×1800 sec. The rms noise of the final 1-d spectra is approximately 10^{-4} of the $H\beta$ flux.

For the analysis we selected several (8–9) strong and well exposed lines which cover a broad range of excitation potentials. This allows us to probe the whole nebular depth from the highly ionized inner regions ($\text{He II } 4686\text{\AA}$) to the neutral outer layers ($[\text{O I}] 6302\text{\AA}$). The three pairs O III and Ar IV , S II and N II , and Cl III and S III , each come from very similar region, leaving effectively five independent probes. The SMC PN was unresolved but the other two PNe show line splitting in the low-excitation lines, which indicates they are partially resolved.

3 THE MODEL ANALYSIS

3.1 The computer codes

We applied the 'Torun models' (Gesicki et al. 1996) to deduce the density and velocity radial distribution of our PNe. A brief description of the procedure is repeated here. We emphasize that the models assume spherical symmetry (as do most photo-ionization models) and this is likely to be the limiting approximation.

The central star is approximated by a black-body atmosphere defined by an effective temperature and a luminosity. The nebula is approximated as a spherical shell defined by an inner and an outer radius, a total mass and a radial density distribution. A photo-ionization model is calculated to fit the (published) line ratios, $H\beta$ flux, and electron density and temperature. We adopt published values for the metallicity. The model is used to calculate predicted surface brightness profiles, which are compared to published

monochromatic images. The model is iterated until an acceptable agreement is found: the main 'free' parameters in this iterating procedure are the radial density distribution and the central star parameters. For every line under consideration, a radial emissivity distribution is calculated.

Subsequently a radial velocity profile is assumed, with the velocity varying smoothly with radius. At every radial position, the line profile is calculated from the local velocity (and turbulence), the local electron temperature and the local emissivity. For every point on the image of the nebula, we calculate a total line profile by integrating along the line of sight. The observed line profile is obtained by masking the model nebula using the slit parameters, and summing over this slit. The seeing is taken (approximately) into account as an additional broadening of the slit. Comparing the predicted profile with the observations now allows one to correct the assumed velocity field. In addition to the velocity profile, a turbulent component can also be included. New to the Torun models is the possibility to allow for a radially varying degree of turbulence.

In the Torun models, the radial velocity is specified at an arbitrary number of positions. These are fitted using smoothed cubic splines. In previous papers, relatively simple velocity profiles were applied. Here we investigate the velocity fields in much more detail than has been possible before.

3.2 The applicability of models

Because spherical symmetry is built into our (photo-ionization) models we restrict the analysis only to those objects which are not too far away from appearing circular. Although many PNe show very complicated structures, both in images and spectra, near-spherical PNe still constitute a significant subset of all PNe with known shapes. Depending on the definition their fraction is estimated as between 10% and 25% (Soker 2002). The fraction of objects suitable for our analysis can be much broader if we include moderately elliptical PNe.

An example of a prolate ellipsoidal PN is NGC 7027, with an axial ratio of 2:1. Long-slit echelle observations show that the same velocity law applies to both nebular axes (Walsh et al. 1997a). Hydrodynamical calculations of aspherical PNe (Mellema 1995) find uniform expansion in all directions. These observational and theoretical findings suggest that our spherical velocity modelling can be applied to mildly elliptical nebulae, which constitute of the order of 50% of known objects. Bipolar objects, which can have high-velocity polar flows, should be avoided especially when integrated spectra are used. The presence of bipolar flows is often evident from integrated spectra. In earlier applications of the Torun models objects with marked bipolarity were always excluded.

The velocity accuracy of our method is restricted by the spectral resolution of the observations, limited by the spectrograph and the thermal line widths. In the present work we cannot resolve details smaller than about 5 km s^{-1} . The spatial resolution of our modelling is limited by the apparent size of the PNe which is comparable to both the size of the slit and the seeing. Because of these observational limitations the analysis must be restricted to large scale structures

and flows, and small inhomogeneities cannot be addressed. This also argues against attempting bipolar nebulae.

In the next sections, describing each single PN, we discuss the available images. There is some evidence for deviations from sphericity: Wray 16-423 may show elongation, SMP 5 is circular but could be a flattened shell seen face on (suggested by the fact that the central brightness is not well fitted), and M 2-31 appears circular. We find no evidence of marked bipolarity in images, and the regular line profiles show no indications of (bi-)polar flows.

Using a radiation-hydrodynamic code, Mellema (1997) suggests that bipolar nebulae much easier evolve around higher mass central stars ($0.836 M_{\odot}$) while lower mass stars ($0.605 M_{\odot}$) tend to produce elliptical PNe. This is because the less massive star evolves slower, giving the density distribution in the surrounding shell time to smooth out. Anticipating our results presented later, the fact that our central stars have masses close to the lower value favours an elliptical shape over a bipolar one.

3.3 The modelling procedure

The velocity field is obtained by trial and error; we cannot be certain that the solutions are unique. Nevertheless we always start with the simplest possible field, i.e. constant velocity. While comparing the computed profiles with the observed ones, taking into account the earlier calculated ion stratifications, we change the velocities at different radial distances to obtain the required change in profiles. We always search for the simplest solution which improves as much as possible all reliable residual in line shapes. We illustrate this procedure in detail when discussing the first object; for the other two PNe we skip this step and show only the final results.

Tables 1 and 2 summarize the input parameters of the three modelled PNe. They also list some models results and compare them with literature data. For the comparison with the observed T_e and N_e , we list the model values at the radii at which the emissivity of the relevant ion peaks. V_{av} denotes the mean value of the velocity field weighted by the mass distribution (Gesicki et al. 1998). The metallicity listed as [O/H] in fact presents the average of [Ne/H] and [O/H]: neon follows oxygen very closely in the ISM (Henry 1989) with identical production sites, but oxygen in PNe can be affected by 3rd dredge of primary oxygen, especially at low metallicity (Péquignot et al. 2000).

The individual objects are discussed extensively in the following sections, where literature references are given. Each section begins with a description of the nebula, followed by subsections on the density distribution and the velocity field.

4 WRAY 16-423 (PN G 006.8–19.8)

4.1 The nebula

The planetary nebula Wray 16-423 is located at a distance of 25 kpc in the Sagittarius Dwarf Galaxy (Zijlstra & Walsh 1996). The PN has a well-determined progenitor mass ($1.3 M_{\odot}$) and metallicity ([Fe/H] = -0.55). The central star shows a weak [WC] (wels) spectrum. The other known PN in this galaxy, He 2-436, shows strong [WC] lines (Walsh et al.

1997b). Originally, Wray 16-423 was classified as [WC8], but Dudziak et al. (2000) show that this was based on a wrong C III identification: the type is considerably earlier, in better agreement with the high effective temperature.

A photoionization model study of Wray 16-423 has been published by Dudziak et al. (2000), where a detailed chemical composition is derived. Their final model which fits all observed line ratios is a composite of optically thin and thick components. We adopt their chemical composition; some of their data are given in Table 1.

For our work we selected 9 spectral lines (presented by open circles in Fig. 2). Some of these, especially [O I], indicate the presence of an asymmetry in this PN. O III and radio images (Dudziak et al. 2000) indicate a partially resolved, elliptical nebula, with a major axis around $1''$ and a (more uncertain) minor axis of $0.7''$.

4.2 Size and density distribution

The observed angular radius of $0.5''$ (Walsh et al. 1997b), at the distance of 25 kpc, corresponds to 0.06 pc. The high excitation lines (He II, [Ar IV], [O III]) do not show line splitting, confirming that the (inner) emitting region is smaller than the slit width. However, lower-excitation lines do show some line splitting, and must form in a more extended region. We adopt an outer radius of 0.09 pc ($0.75''$), and a density structure for which the calculated surface brightness in $H\beta$ decreases to 10% of maximum at $0.5''$. Our photoionization code gives line ratios close ($\sim 50\%$) to the values given in Dudziak et al. (2000). However, there is a noticeable difference between the electron density estimated from observed [S II] line ratios (Walsh et al. 1997b) and that in the outer layers of our model. Dudziak et al. (2000) model Wray 16-423 with two sectors: for their lower-density sector they find $N_e = 3600 \text{ cm}^{-3}$ which is in between our and Walsh et al. values. A high-resolution image of a low-excitation line could resolve this issue, but no such image is presently available. The model is ionization bounded.

4.3 Velocity fields

We begin the discussion of the first nebula with an overview of simple velocity fields, to illustrate the procedure to obtain an acceptable model. The results of the initial models are shown in Fig. 1. We show only six lines in the plot, nevertheless the chosen lines represent the whole nebula. The constant-velocity-field model is presented in two versions: without and with additional turbulence. The short-dash line presents the non-turbulent solution: the value of 25 km s^{-1} is on average the best value. To show how additional turbulent motions change the line shapes we compute the same model with a very high turbulence of 15 km s^{-1} . The dotted line presents this exaggerated case; it shows that the line wings are broadened and simultaneously the maxima are smoothed to a Gaussian shape. Both cases fail for almost all lines.

Before modifying the velocity we look at the lower right panel of Fig. 1 showing the radial distributions of emissivities. Again not all nine lines are presented because several distributions almost overlap and $H\beta$ follows closely the density shown in the next panel. Fig. 1 indicates the radii of formation of considered lines, i.e. the radii where the line profiles are most sensitive to changes in velocity.

Table 1. Parameters of the nebular models compared with observed values

object	M 2-31 PN G 6.0-3.6	SMP 5	Wray 16-423 PN G 6.8-19.8
distance [kpc]			
from literature	4.75	60.3	25
assumed in model	8.0	60.3	25
NEBULA			
Angular diameter [arc sec]			
from literature:	opt. 2.1, radio 3.8	opt. 0.5	opt. 1.2, radio 0.7×0.3
from model H β image	2 core, 3.6 halo	0.5 core, 1 halo	1 core, 1.5 halo
model outer radius	2.2 10 ¹⁷ cm (0.07 pc)	4.7 10 ¹⁷ cm (0.15 pc)	2.8 10 ¹⁷ cm (0.09 pc)
model inner radius	0.16 10 ¹⁷ cm	0.47 10 ¹⁷ cm	0.28 10 ¹⁷ cm
extinction c(H β)	1.34	0.097	0.21
log F(H β)			
observed, dereddened	-10.57	-12.65	-11.89
calculated from model	-10.6	-12.56	-11.73
[O III] electron temperature [K]			
from literature	10100, 9890	13629	12400
from our models	9740	13100	12380
[N II] electron temperature [K]			
from literature	11400, 9775	–	
from our models	10400	11600	12350
[S II] electron density [cm ⁻³]			
from literature	4030, 5050	–	6000
from our models	4490	790	1290
V _{exp} [km s ⁻¹] observed			
[O III] peak separation	9	–	–
[O III] HWHM	25	19	23
[N II] peak separation	23	–	21
[N II] HWHM	35	23	–
V _{av} [km/s] calculated from model	30	30	33
additional turbulent broadening [km/s]	10–20	0	0
ionized mass [M _⊙] calculated from model	0.26	0.61	0.33
metallicity [O/H]	–0.2 :	–0.6	–0.55
STAR			
spectrum description	[WC 4-6], wels	–	[WC 4–6], wels
log(T _{eff}) from literature	4.8, 4.9	5.14	4.95 or 5.1
log(T _{eff}) adopted	4.86	5.14	5.0
log(L/L _⊙) from literature	3.6, 3.5	3.77	3.66 or 3.7
log(L/L _⊙) adopted	3.7	3.61	3.7
estimated dynamical core mass [M _⊙]	0.62	0.61	0.61

The largest discrepancies exist for low excitation lines, indicating a required increase of the velocity in the outer region. The long-dash line shows the (non turbulent) monotonic velocity field which usually was assumed (Gesicki et al. 1998) and which is predicted from hydrodynamic models (Marten & Szczerba 1997, Perinotto et al. 1998). The new fit shows clearly that this is the appropriate way to reproduce the low excitation outermost lines. The acceleration in the outermost layers is connected with the ionization front, and is a known, common feature of PNe (Acker et al. 2002).

As a new result, the monotonic velocity field also fails at the highest excitations in Wray 16-423. The He II line is too broad: a high velocity (50 km s⁻¹), high density region

is required near the inner nebular radius. Further out the velocity must decrease significantly (to about 15 km s⁻¹) to reproduce the narrow cores of the [O III] and [Ar IV] lines. The outer regions accelerate to 60 km s⁻¹, and must show a density decreasing with radius, otherwise the high velocity wings become too pronounced. A constant density halo can be ruled out.

This velocity field is shown in Fig. 1 as the solid line. The general shape of all 9 lines is reproduced (see the Figure), but it is clearly visible that a number of lines with intermediate excitation ([S III], [Cl III], [O III], [Ar IV]) have broader wings than the fit predicts. This shows that a component expanding at about 40 km s⁻¹, at intermediate radii,

Table 2. Comparison of observed (dereddened) and calculated line ratios, relative to $I(\text{H}\beta) = 100$

line	M 2-31			SMP 5			Wray 16-423	
	PN G 6.0-3.6						PN G 6.8-19.8	
	observed (1)	model (2)	model	observed (2)	model (3)	model	observed (4)	model
[O II] 3726	–	66	53	80	–	55	19	45
[Ne III] 3868	–	103	132	87	–	69	74	83
He II 4686	–	0	3	41	41	35	11	13
[O III] 5007	1116	973	910	962	–	916	1085	997
[O I] 6300	6	4	4	9	–	4	2	2
[S III] 6311	3	–	2	–	–	1	2	2
[N II] 6584	60	77	93	25	–	22	18	37
[S II] 6717+6731	13	11	13	9	8	8	5	6
[Ar III] 7136	17	–	12	–	–	6	10	5

(1) Acker et al. (1991)

(2) Stasinska et al. (1998)

(3) Liu et al. (1995)

(4) Walsh et al. (1997b)

is missing. Adding this additional high velocity component improves the fit significantly. The resulting velocity profile, and the resulting emission line profiles, are shown in Fig. 2. The assumed velocity components have an almost negligible effect on the $\text{H}\beta$ line because (being least massive) hydrogen is strongly thermally broadened.

The 'best model' gives an interesting velocity profile. The velocity spike at $R \approx 0.5R_{\text{out}}$ gives the impression of an embedded shock. If the density is also enhanced in this region, the high velocity region would become even thinner. Alternative possibilities are explored in Section 10.

5 SMP 5

5.1 The nebula

This planetary nebula is located in the Small Magellanic Cloud. A photoionization model is published by Liu et al. (1995), based on optical and UV spectrophotometry and on Hubble Space Telescope images. The data given in Table 1 and Table 2 are taken from this paper. Their model reproduces many observed parameters; however, it fails to fully reproduce the [O III] image: the calculated [O III] surface brightness decreases faster outwards than observed. Another photoionization model is published by Stasinska et al. (1998); their data supplement our tables. The chemical composition is adopted from their paper.

In our echelle spectrum, 8 lines are suitable for model analysis. The observed line profiles are presented by the open circles in Fig. 3.

5.2 Size and density distribution

The $\text{H}\beta$ and [O III] 5007Å images (Liu et al. 1995) show a nearly circular nebula. The azimuthally averaged surface brightness distributions of Liu et al. are shown in Fig. 3 (lowest central box), where the filled circles correspond to $\text{H}\beta$ and the open circles to [O III]. We first tried to reproduce these surface brightness profiles by iterating (trial and er-

ror) the density structure. The result is shown in the same figure, together with the predicted N II distribution.

The $\text{H}\beta$ image shows an outer radius of $0.25''$. The [O III] image is somewhat larger, and peaks further out than $\text{H}\beta$ by about $0.04''$. The reason is that the star is sufficiently hot that the innermost region is dominated by O IV (e.g. Leene & Pottasch 1987), up to the density maximum at $0.1''$ radius. The observed [O III] emission remains brighter than $\text{H}\beta$ in the outer regions. This can be expected in density-bounded nebulae, where the O III zone extends to the outer radius. But in such density-bounded models, the [O I] 6300Å line intensity is about 10^{-4} of $\text{H}\beta$, much fainter than observed. SMP5 appears to be ionization-bounded.

To fit both the extended [O III] distribution and the strength of the [O I] line, we appended a low-density outer region extending out to a distance of $0.5''$. In this model, the [O III] zone terminates at a radius of $0.4''$. Placing the ionization front still farther out could reproduce the tail of the [O III] distribution even better, but its radius cannot be much larger than $0.5''$: otherwise the [O I] 6300Å line would be expected to show line splitting, which is not observed.

Increasing the stellar T_{eff} would shift the [O III] image still farther out but it is not an overwhelming improvement: we adopted the temperature of Liu et al. (1995). We obtain a better fit to the brightness distribution than Liu et al.: they use a slightly higher density than ours, resulting in a smaller ionization radius. In our model, the outer region should be visible in the 6585Å [N II] line. An image at this wavelengths could decide between the two models. Without such an image, the halo is in essence a free parameter in our modelling. We note that our model fails to fit the image details in the very central region.

A consequence of the assumed outer region is the high nebular mass of $0.61 M_{\odot}$, much higher than $0.194 M_{\odot}$ obtained by Liu et al. (1995). Nevertheless the $\text{H}\beta$ flux and the line ratios are well reproduced.

tentative models of Wray 16-423

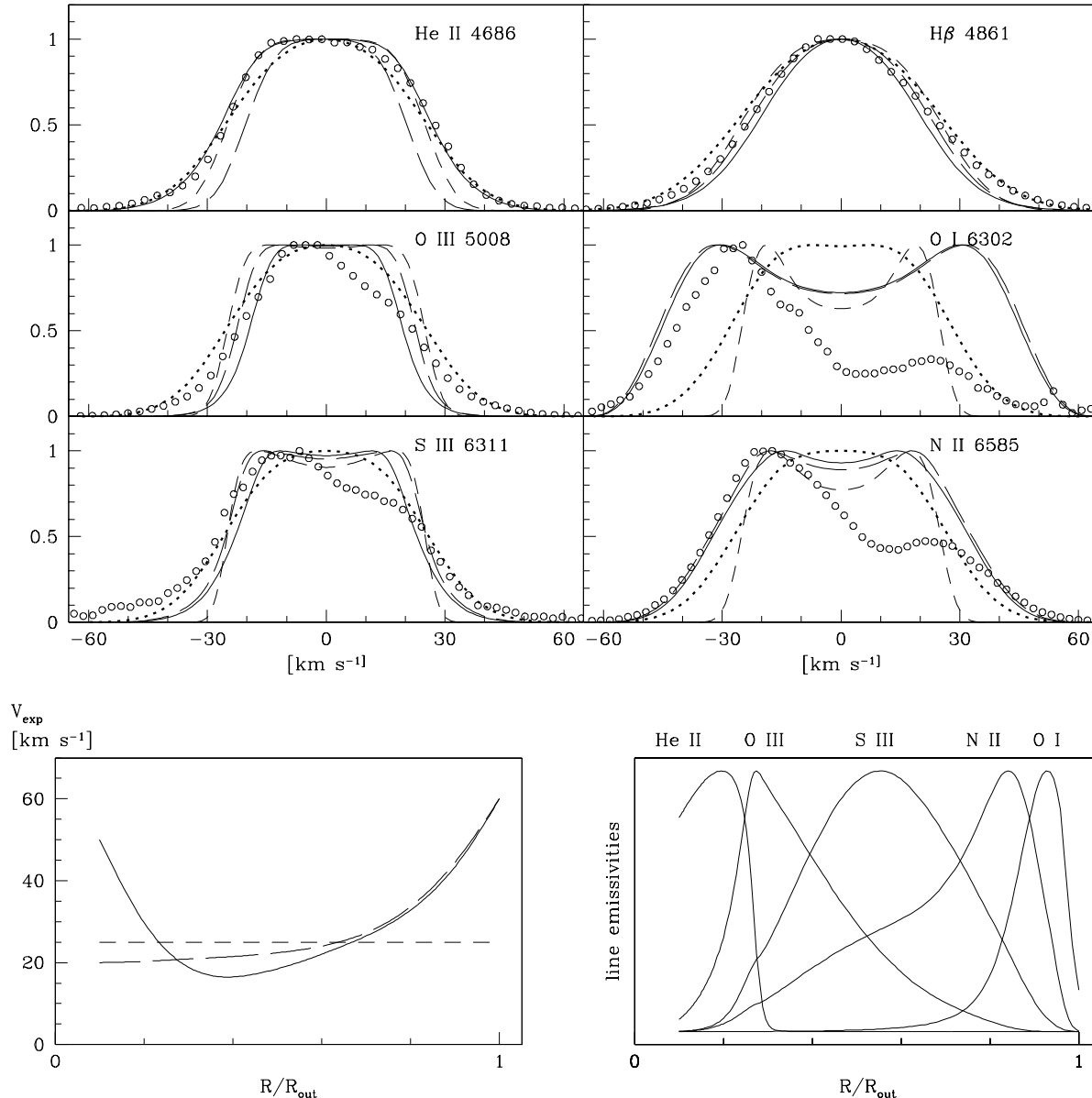


Figure 1. Examples of rejected models: the observed and modelled lines and model parameters for Wray 16-423, using over-simplified velocity fields. The upper panels present six representative emission lines; the points correspond to the observations, and the lines to the calculated models. The intensities are normalized to unity. The velocity scale is given in the lowest boxes. In the lower left panel, the different velocity fields are marked with different line types, corresponding to the emission lines shown above. The right panel shows the radial emissivity distribution in selected lines. More explanation is given in the text.

5.3 Velocity field

The different emission lines show different line widths. Assuming the halo has constant density, or slightly decreasing like in Wray 16-423, causes the maxima of the emissivity distribution of all lines to be contained in the dense central region. But the different line widths indicate the line emission regions are well separated. Introducing a small density increase outwards shifts the low excitation lines outwards, as required. The N II, S II, S III ions now exhibit two emissiv-

ity maxima: one connected with the density maximum, the other with the ionization stratification in the outer region.

The He II line is broader than [O III] and [Ar IV] which implies an increase of the velocity towards the central star. The width of the [O I] line indicates acceleration at the outer nebular radius. A flat-top line profile results from a spatially unresolved layer expanding with constant velocity (Gesicki & Zijlstra 2000). The narrow flat tops of the [O III] and [Ar IV] lines indicate the presence of such layers in the inner dense layers, with a low expansion velocity of about

Wray 16-423

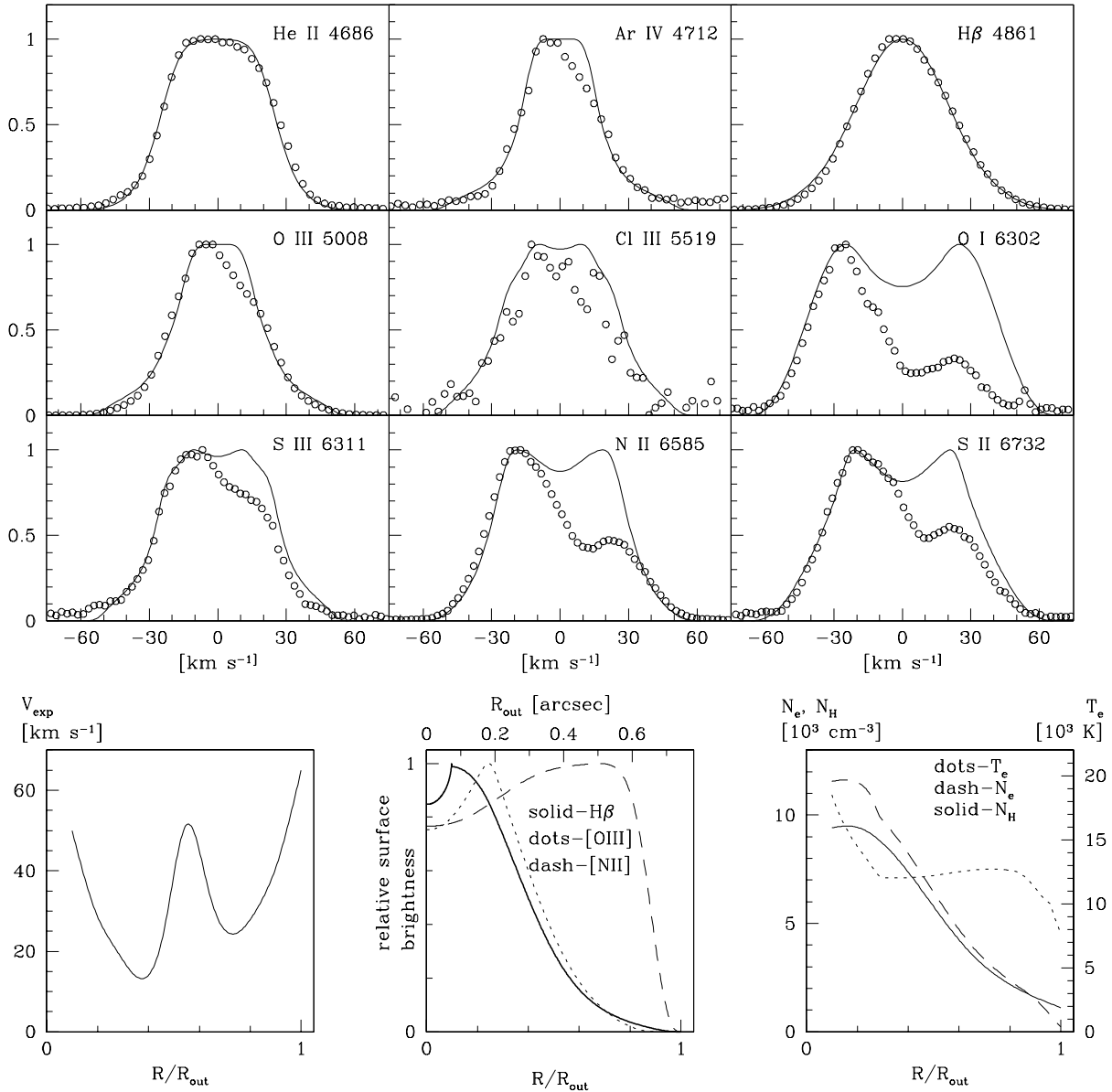


Figure 2. Observed and modelled lines and model parameters for Wray 16-423. The upper panels present the nine emission lines; the points correspond to the observations, and the solid curves show the calculated models. The intensities are normalized to unity. The velocity scale is given in the lowest boxes. The lower panels show the model structure as function of the relative radius. In the left panel, the velocity field is shown. The central panel shows the model surface brightness profiles. The right panel shows the assumed density distribution together with the model electron temperature and density curves.

15 km s^{-1} . Similar flat tops in the [O I], [N II], [S II] lines indicate another velocity minimum at about 20 km s^{-1} in the outer layers. The line wings, which extend over 50 km s^{-1} , require a velocity maximum in between. Any velocity field simpler than shown cannot reproduce all selected lines simultaneously.

6 M 2-31, (PN G 006.0-03.6)

6.1 The nebula

This PN is likely located in the Galactic Bulge. Van de Steene & Zijlstra (1994) estimated the distance as 4.75 kpc. Dopita et al. (1990) adopted 7.8 kpc assuming that M 2-31 is a Galactic Bulge nebula. We obtain a better fit using this larger distance (see below).

The central star is classified as [WC 4-6] by Tylenda et al. (1993) but as 'wels' by Parthasarathy et al. (1998).

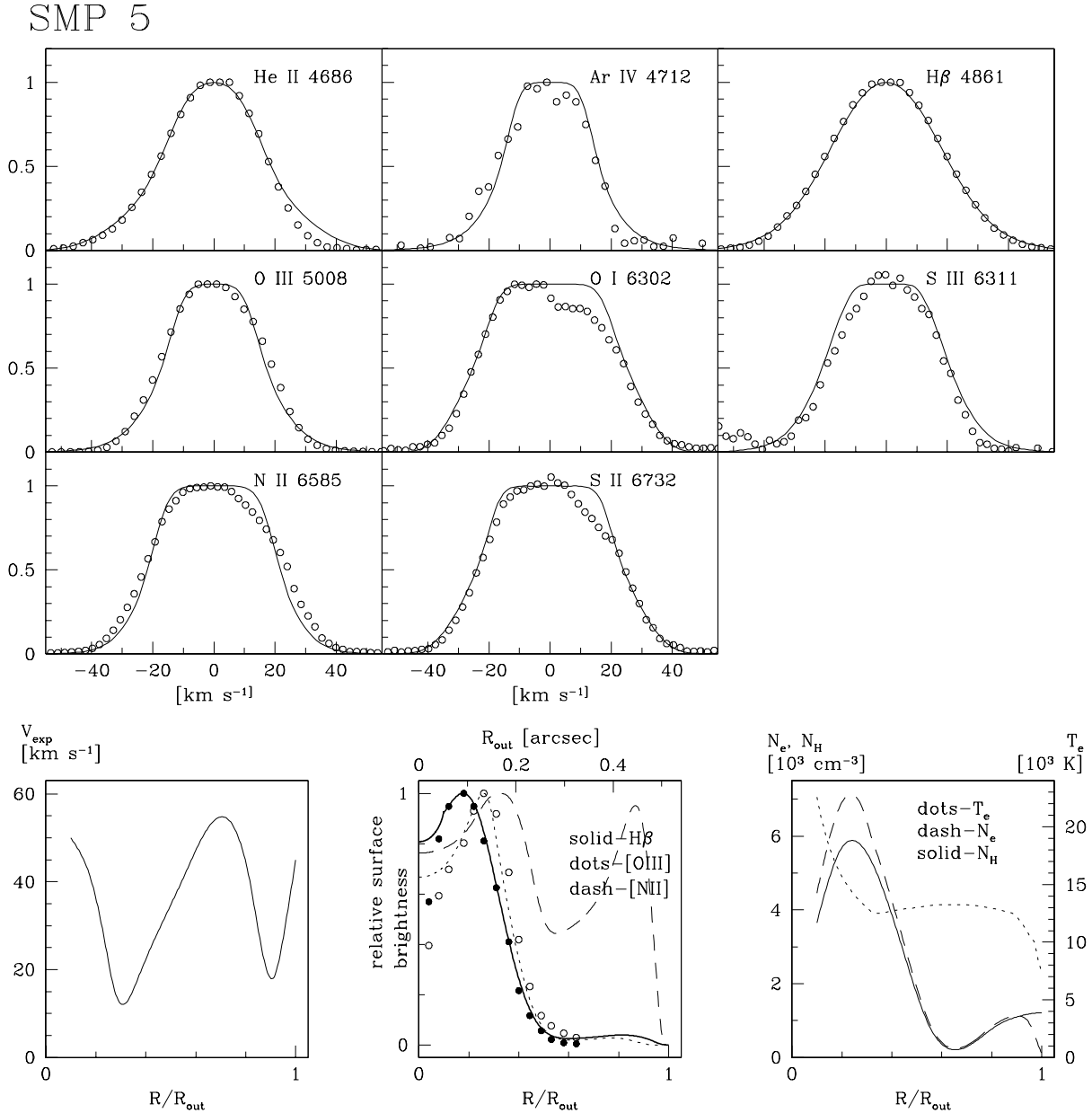


Figure 3. Observed and modelled lines together with model parameters of SMP 5. The arrangements are the same as in Fig. 2, but only a single velocity solution is shown, and in the relative surface brightness box the observed points are overplotted.

PNe with [WC]-type central star show a tendency towards strong turbulent motions: the evidence for this comes from Gaussian line shapes which are of comparable width for all species (Gesicki & Acker 1996, Acker et al. 2002)¹. The first evidence for turbulence was based on line profiles of [N II], H α and [O III] (Gesicki & Acker 1996). Additional lines later yielded much stronger constraints on the presence of turbulence (Neiner et al. 2000). We cover similar lines to Neiner et al., but at 50% higher resolution and with higher S/N.

¹ A Gaussian shape for a single line can be fitted using radially increasing velocities, but this does not produce the same width for all lines.

Photoionization studies of M 2-31 have been published by Acker et al. (1991) and Stasinska et al. (1998); their results are given in Table 1 and Table 2. The chemical composition is adopted from Stasinska et al. (1998). The abundances may be more uncertain than in the previous two PNe: the [Ne/H] is about solar while the [O/H] = -0.4 dex (see Stasinska et al. 1998): Ne and O are expected to follow closely similar abundance patterns (Pequignot et al. 2000, Henry 1989) and the large difference would need confirmation.

A very high-resolution [O III] 5007Å image, and spectrophotometry data are published by Dopita et al. (1990);

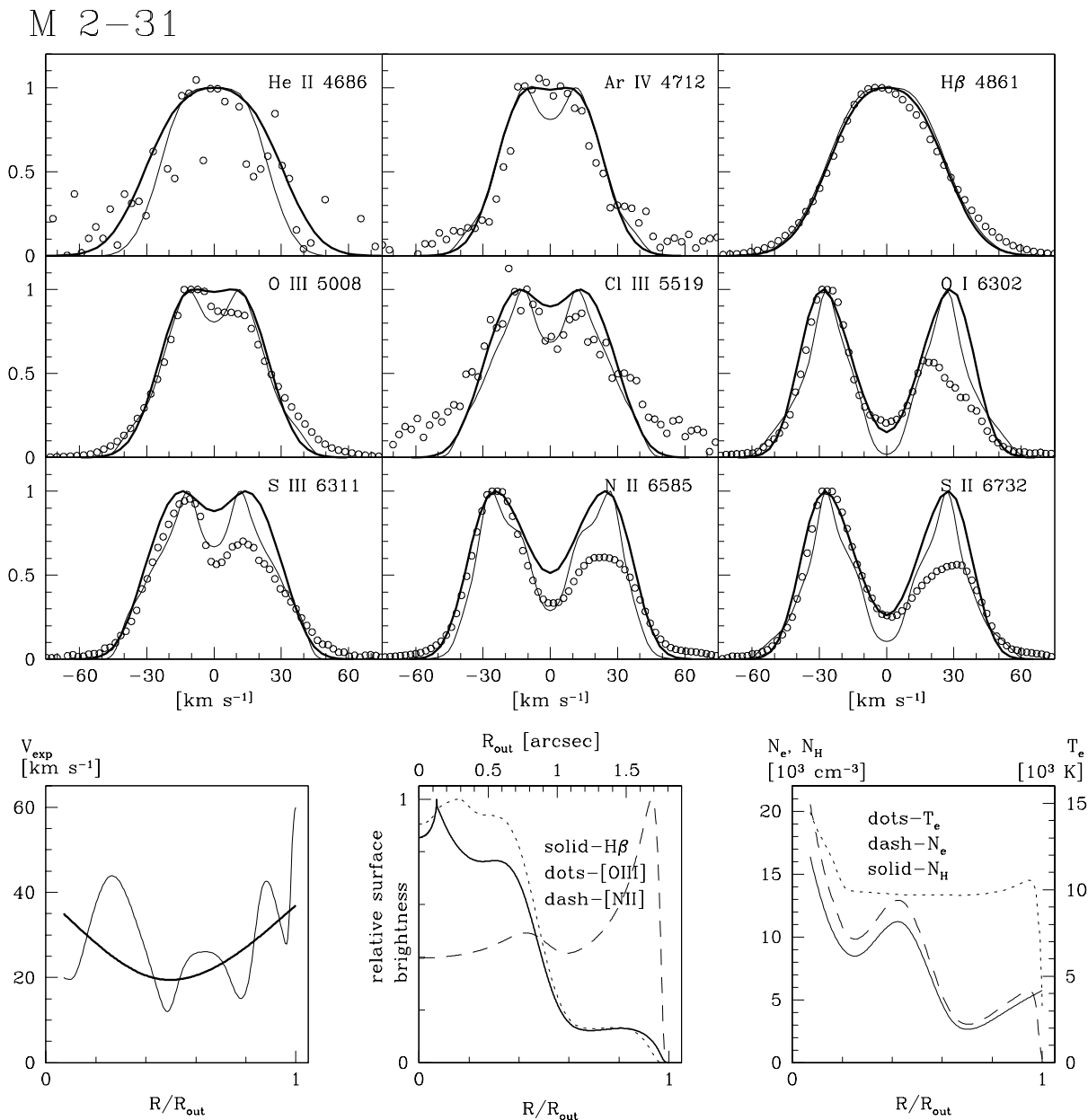


Figure 4. Observed and modelled lines together with model parameters of M2-31. The arrangements are the same as in Fig. 2.

they also present a photoionization model analysis. A radio image is published by Gathier et al. (1983).

For our analysis we selected 9 spectral lines, presented by open circles in Fig. 4. We include the He II line despite its low signal to noise: it is the only available probe for the innermost nebular layers.

6.2 Size and density distribution

We first attempted to obtain a photoionization model using the smaller statistical distance (Van de Steene & Zijlstra 1994): this was rejected because to fit the line ratios and $H\beta$ flux, the model nebula has a very small ionized mass and the central star a very low luminosity. This can not be

a priori excluded, but at the Galactic Bulge distance these parameters become more regular (see Table 1) and this was therefore considered more likely.

The assumed distance determines the nebular physical radius. The [O III] 5007Å image of Dopita et al. (1990) shows a diameter of about $2.2''$ and is flat-topped, without a central hole, and with steep edges. The radio image of Gathier et al. (1983) shows the brightness increasing steadily towards the center; the diameter is estimated as $2.1''$. Zijlstra et al. (1989) estimated from the same image the diameter as $3.8''$.

The dimensions of the spectrograph slit were $3'' \times 1''$. In the observed spectrum the high excitation lines are unresolved while the low excitation lines are clearly resolved. This confirms the presence of ionization stratification, where

the central nebular regions (traced by O III and Ar IV) are confined within the slit width, while the outer regions, traced by the lower ionization stages, extend beyond the slit. We adopted an outer radius of $1.8''$ but searched for a model producing a much smaller [O III] image.

The observed structure can be modelled with the density distribution shown in Fig. 4. To reproduce the [O III] image without a central hole it is necessary to assume a very small radius of the empty inner cavity, with density higher towards the center. To obtain a flat-topped image out to $0.4 R_{\text{out}}$, we need to also increase the density outside the [O III] dominated region. We implemented this as a high density bump near $0.4 R_{\text{out}}$. Now the [O III] image is almost flat-topped (it shows some structure at intensities $0.9 < I/I_{\text{peak}} < 1.0$), and decreases to 10% of maximum near $0.6 R_{\text{out}}$ which is comparable to the observations.

For $R > 0.7 R_{\text{out}}$ the density in the model increases again. This assumption, similar to the case of SMP 5, was needed to shift the low excitation lines to the outer nebular regions to reproduce the splitted line profiles. Also, without such a density increase the calculated [O I] 6300 Å line would be too weak, compared to the observed line ratios. These remote layers do not enlarge the [O III] image. The outer nebular radius must correspond to an ionization front: in a density-bounded model the lines of ions [O I], [N II], [S II] become too weak.

6.3 Velocity field

The line emissivity distributions show complicated radial structure. The high excitation lines show two closely-spaced emission peaks, corresponding to the two inner density maxima. The outermost low excited lines emit mostly near the outer radius. The intermediate-excitation ions Cl III and S III exhibit two well-separated emission maxima: they are not affected by the density maximum at the inner edge.

No simple velocity field can explain the observed lines. Being encouraged by the shocked velocity field of SMP 5 we tried to find something similar. Without additional turbulence, the best fit for all 8 lines can be achieved with the 'wavy' velocity curve presented by the thin line in Fig. 4. The very outer velocity increase is again naturally explained by the presence of the ionization boundary. The innermost velocity is not probed even by the He II ion. We assumed a velocity decrease in this region, which could be associated with the strong increase of density towards the center, and is also consistent with the not very broad (but noisy) He II 4686 Å line.

A concern of this fit is that the number of extrema in the velocity field is similar to the number of independent probes (see Section 2). Fig. 4 shows some residuals are still present in the modelled lines despite the elaborate velocity profile. The observed emission lines are clearly smooth in shape: higher-order components would be needed in the velocity field to fully reproduce the spectral lines. Such a situation occurs more naturally when the velocity field is dominated by turbulence. Therefore we searched for another best fit model, assuming the simplest possible velocity field and including turbulent broadening of lines.

We cannot find a satisfactory fit with the linear velocity field found for many WR planetaries (Acker et al. 2002): the [Ar IV] and [O III] lines show clearly a smaller expansion

velocity than [O I], [N II], [S II]. The best and the simplest fit is obtained with a parabola-like velocity field, shown in Fig. 4 by the thick line. The expansion velocity must be near 20 km s^{-1} at the intermediate radii, while the [O I] line indicates a velocity increase outwards, and the extended wings of the [O III] lines indicate an increase inwards. The best fit is obtained with a turbulence which is also varying, decreasing from 20 km s^{-1} at the inner radius to 10 km s^{-1} at the outer edge.

Neither velocity field gives as good a fit as found for SMP 5.

7 CENTRAL STARS

We selected three objects from very different stellar populations, with different metallicity and progenitor mass. The distance is known for all three objects, allowing us to calculate the luminosity. The results listed in Table 1 show that all three have a closely similar value of $\log(L/L_{\odot}) \approx 3.7$. Because of the steep core-mass-luminosity relation (Herwig et al. 1998), this implies that the core masses are also very similar. The stars are hot: 70 kK for M 2-31, 100 kK for Wray 16-423 and 140 kK for SMP5. The temperatures scale well with the outer radii, of 0.07 pc, 0.09 pc and 0.15 pc, respectively: the hotter the star, the more evolved the nebula. The ionized mass increases in the same sequence. These similarities suggest that the three stars are evolving on very similar evolutionary tracks.

Gesicki & Zijlstra (2000) describe a way to derive the core mass from the dynamical nebular age and the stellar temperature. This yields the time scale on which the central star reached its present temperature, and this evolutionary time scale is highly sensitive to the core mass. The dynamical age is calculated from the mass-averaged expansion velocity and the outer radius. A metallicity-dependent correction is applied to allow for the slower original AGB expansion. The resulting dynamical core masses are $0.61\text{--}0.62 M_{\odot}$ (Table 1), confirming that the stars are evolving on almost identical tracks. The masses fall at the peak of the distribution for the Bulge (Gesicki & Zijlstra 2000).

The initial masses are likely different. The Bulge PN can be expected to have an old, $1 M_{\odot}$ progenitor. The age of both Sgr PNe is derived as 5 Gyr (Dudziak et al. 2000), giving a progenitor mass of $M_i \approx 1.3 M_{\odot}$. The value for the SMC PN is not known, but its metallicity is very high for the SMC, which indicates a relatively young object, with $t < 3$ Gyr (Piatti et al. 2001, Dolphin et al. 2001). SMP 5 is located in the bar of the SMC, in a region where the recent star formation (within the past Gyr) has taken place (Van den Bergh 2000). This suggests a fairly massive progenitor. (The sequence of initial masses is the same as the stellar T_{eff} , nebular radii and ionized masses.) But the different values for M_i have not resulted in different core masses. The core mass at the first helium flash is almost independent of progenitor mass, for the range $1 < M_i < 2.5 M_{\odot}$. The difference between this core mass and the final mass is determined by the mass-loss efficiency (Vassiliadis & Wood 1993, Blöcker 1995).

Two of the stars show [WC]-type characteristics. However, their stellar parameters are not obviously different from the non-[WC] star. This lack of correlation has also been

found for a study of Galactic [WC] stars (Górny 2001). Acker et al. (2002) and Mellema (2001) discuss the link between nebular turbulence and [WC] hydrogen-poor winds.

The inner radii of the nebulae are very small (Table 1). The inner radius is determined by the pressure from the hot wind from the central star (Mellema 1994); the small values suggest our stars have had relatively weak winds. The present [WC] characteristics of two objects show the presence of a stronger wind; the very hot star of SMP5 will also have a stronger wind (Pauldrach et al. 1988). The appearance of the nebulae suggests that these winds may have only developed recently. Stasinska et al. (1998) studied PNe in five galaxies, and concluded that, on the horizontal post-AGB/PN track, the central stars in the Magellanic Clouds PNe evolve more rapidly than predicted by models of Blöcker (1995), which could help explain the small inner radius.

8 PROPERTIES OF THE VELOCITY FIELDS

8.1 Non-monotonic velocity structure

The present results show evidence for complicated velocity fields (assuming spherical symmetry: this is explored further below). Previously, the velocity fields were modeled as monotonic increasing with radius, approximately as r^2 often with strong acceleration at the ionization front. For [WC]-type PNe, a constant velocity with supersonic turbulence (see e.g. Acker et al. 2002) was found. Such simple velocity fields do not fit the PNe studied here.

It is likely that the present PNe are not unique in this. The earlier analyses summarized in Acker et al. (2002) were based mainly on two or three spectral lines, and were only sensitive to simple velocity fields. Some indications of more complicated velocity field were noticed in Neiner et al. (2000). They observed 8 PNe (of which 5 with [WC] central stars) in up to 10 emission lines at a resolution of 42 000; the data were analyzed with the Torun models. They report three cases where the [O III] 5007Å and some other lines are clearly not well reproduced by the models. However, almost all of their nebulae show smaller deviations from the models: at higher resolution and better S/N, evidence for more complicated velocity fields could have emerged for some of these objects as well. The two samples together suggest that at least 50% of PNe, and possibly a much higher fraction, show evidence for more complex, non-monotonic velocity fields.

The present sample benefits from the presence of high-quality monochromatic images. These allow us to determine small structures in the radial density distribution. In the earlier analysis we very often assumed a simplified density field because of the absence of detailed images. For our three PNe we find indication for dense inner shells and lower density outer regions. The improved density structure aids the more detailed velocity analysis.

8.2 Turbulent velocity structure

The presence and importance of turbulence in PNe with [WC]-type central stars is well established. Acker et al. (2002) fit the line profiles of these nebulae using a constant

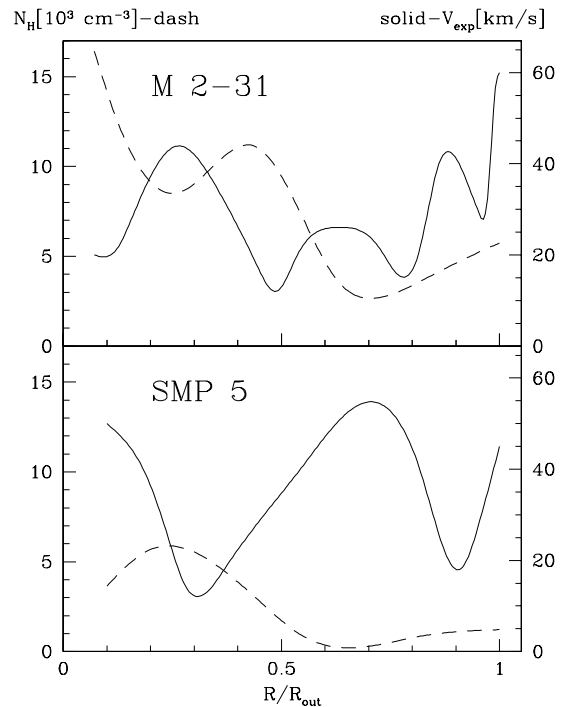


Figure 5. The density and velocity fields for M 2-31 and SMP 5

expansion velocity, and a turbulent component also independent of radius. It can be expected that in reality, both components are varying with radius, but up to now the data was insufficient to explore this further.

For one of the [WC]-type PNe in our sample, M 2-31, we propose two velocity solutions with the same density structure. The clearly splitted lines of the low excitation ions exhibit an obvious Gaussian shape, indicative of turbulence. The wings of other lines are also well fitted with the turbulent model. This supports the statement of Acker et al. (2002) that PNe around WR planetaries suffer from turbulent-like motions which are additional to thermal turbulence. Nevertheless, the non-turbulent, 'wavy' solution also fits the line profiles. The two velocity curves are shown in Fig. 4: the 'wavy' line follows the smooth one, and the amplitude of the fluctuations is comparable to the turbulence value. The number of waves is the same as the number of excitation region which we probe. This suggests that the actual velocity structure may occur at an even smaller scale. This situation approaches the semantics of turbulence. The turbulent solution is simpler and therefore more elegant.

(The other [WC]-type PN, Wray 16-423, shows no evidence for turbulence. It has a weaker [WC] feature and may be classified as *wels*.)

The non-turbulent, 'wavy' solution shows one characteristic which the turbulent solution by its nature hides. Fig. 5 shows the density and non-turbulent velocity distribution superposed. The velocity distribution shows an anti-correlation with the density, in the inner regions. A similar anti-correlation between density and velocity is seen for the non-turbulent SMP 5 (Fig 5).

9 COMPARISON WITH HYDRODYNAMICS

9.1 Published models

Hydrodynamical models have been developed to investigate the effects of interacting winds in planetary nebulae (Kahn & West 1985) and the related shaping mechanisms (e.g. Mellema 1994). A three-wind hydrodynamical model was developed by Schmidt-Voigt & Köppen (1987). Schönberner and collaborators have further developed these models to study the complete evolution of PNe, including the full mass-loss history, interacting winds, and photoionization, for self-consistent stellar evolutionary tracks. These are the ideal models for comparison with the present results. However, only one evolutionary sequence of these highly intensive computations has so far been published, in Perinotto et al. (1998) (who also discuss the history of these models) and Corradi et al. (2000a). The model is calculated for a star with core mass $M_c = 0.605 M_\odot$ (Blöcker 1995), very close to the core masses of the three PNe in this paper. The first three models from their evolutionary sequence, (corresponding to ages of 1776, 4603 and 5462 years counted from the end of AGB) have sizes and densities similar to our PNe.

We briefly summarize the first phases of evolution presented in the two mentioned papers:

- At epoch 1 (1776 years) the model nebula has almost constant density ($\rho \sim 10^4 \text{cm}^{-3}$) up to the ionization front ($r \sim 10^{17}$ cm) where both density and velocity sharply increase.
- Between epoch 1 and 2, the ionization front breaks through the dense swept-up shell and the full circumstellar envelope ionizes.
- At epoch 2 (4603 years) an inner denser shell ($\rho \sim 5 \cdot 10^3 \text{cm}^{-3}$) begins to develop, as a result of the pressure from an inner 'hot bubble'. The hot bubble is due to a shocked hot wind from the star. The outer nebular shell, which is the remnant of the dense shell of epoch 1, has a density $\rho \sim 2 \cdot 10^3 \text{cm}^{-3}$; at its outer edge ($r \sim 3 \cdot 10^{17}$ cm) a shock wave is running into the ambient slow material. The density spike caused earlier by the ionization front, and located at the outer edge, has almost disappeared.
- At epoch 3 (5462 years) the central star approaches its maximum temperature. The nebula shows a pronounced double shell structure. The outer shell, extending to $r \sim 5 \cdot 10^{17}$ cm, has a nearly constant density ($\rho \sim 10^3 \text{cm}^{-3}$): this is the swept-up AGB wind. The inner layers have a three times higher density with a pronounced maximum of $\rho \sim 3.5 \cdot 10^3 \text{cm}^{-3}$ at its inner edge ($2 \cdot 10^{17}$ cm) and a much weaker maximum at its outer edge ($2.5 \cdot 10^{17}$ cm).

9.2 Observed density structures

In our PNe, the inner cavity radius is about 10% of the outer shell radius. In the hydrodynamical models the inner radius of ionized nebula is about 50% of the outer radius. This difference suggests that the transition from AGB to post-AGB wind occurred different from Schönberner's scenario. In subsection 7.1 we suggested that the fast wind may have been weaker than assumed in the hydrodynamical models. Alternatively, the star may have evolved faster (the core mass is slightly higher than in the models) giving the fast wind less time to act, or the AGB expansion velocity may have been

low giving a denser, more compact AGB shell. Perinotto et al. (1998) discuss two sequences differing only in the initial matter distribution. Two snapshots from these sequences, taken at about 1800 years, show a markedly different density distribution. Our experience suggests that the density and velocity distributions would be discernible with the Torun models.

The structure of our PNe, with a high density inner ring and a low density outer region, corresponds to theoretical models 4–5 10^3 years after the AGB. But the models are density bounded while our PNe are ionization bounded. Our PNe have inner rings denser and closer to the central star than the theoretical models. It is possible that the growing density of the inner shell blocked the ionizing radiation and a previously fully ionized PN entered a recombination phase.

Apart from this difference, the epoch-2 model shows a structured dense inner ring with an outer region in which the density slightly increases outwards. Such a situation we met in SMP 5. In the epoch-3 model there is a main density maximum at the inner nebular edge with a smaller but noticeable density bump further out. This situation we found in M 2-31.

9.3 Velocity structures: Making waves

For the first time our analysis led to strongly-non monotonic velocities. It is encouraging that the velocity spikes which we find correspond to features found in hydrodynamical models. However, the intermediate velocity jump can also be interpreted in terms of clumpy structures or asphericity, as discussed later.

Two PNe show a velocity field in a 'W' shape. The velocity distribution for SMP 5 is anti-correlated with the density run (see Fig. 5) as can be expected for gas flows. The hydrodynamical models suggest several processes are responsible for the features in the velocity field.

- The innermost region represents the contact discontinuity between the hot inner region and the PN. It is accelerated by the fast wind of the central star. For a typical mass loss rate of $\dot{M} = 10^{-9} M_\odot \text{yr}^{-1}$ and velocity $v = 10^4 \text{km s}^{-1}$, the energy in the accelerated shell in our models equates to roughly 400 yr of the wind energy. The acceleration can occur through thermal pressure (Schönberner & Steffen 1999) or through direct acceleration of a wind-swept shell (Harrington et al. 1995).
- The outer velocity increase is well understood, and represents the shock driven into the ambient AGB wind by the thermal pressure of the ionized planetary nebula.
- The intermediate shock seen as a weak feature in Schönberner & Steffen (1999) is the compressed AGB wind (a density enhancement) at the outer edge of the inner dense swept-up shell.

The outer velocity increase is seen in all three objects. The innermost increase is seen in two objects; in the third object (M 2-31) it falls in the He III region for which we have no velocity probe. The explanation for these apparently common features appears secure.

The intermediate shock is seen in the same 2 objects (and in M 2-31 may take the form of a superposition of many such shocks). It is not clear that the above explanation as the compressed AGB wind is unique.

Mass-loss variations in the AGB wind could cause density jumps at various radii. An effect of such a jump is in fact present in the models of Corradi et al. (2000a), namely the trace of the last thermal pulse on the AGB, which in the model sequence is located a distance of about 10^{18} cm. The velocity jump associated with this feature grows to about 20 km s^{-1} as the main expanding nebula approaches this structure. This particular feature is not observable, being located in the low-density AGB wind. However, its evolution suggests that any mass-loss fluctuation during the ejection of the main nebula may affect the density and velocity field in the PN. Evidence is emerging that the AGB mass loss fluctuates on time scales of the order 10^2 – 10^3 yr (Hashimoto 1994, Zijlstra et al. 2002).

The turbulence in M2-31 could be interpreted as a special case where instead of a single intermediate shock, many shock-lets are present. The winds from [WC] stars show strong time-variability (e.g. Grosdidier et al. 2000): the variable pressure at the inner edge of the PN could cause a progression of shock waves traveling into the nebula. The velocity amplitude of the observed waves, or the turbulent velocity, is little larger than the sound speed ($\sim 12 \text{ km s}^{-1}$). This suggests an unusual picture of a planetary nebula criss-crossed by a multitude of sound waves.

10 ALTERNATIVE EXPLANATIONS: ELLIPTICAL AND CLUMPY NEBULAE

We should consider the possibility that in our PNe the inner shock found can actually be a spherical approximation to more azimuthally irregular situation. The nebulae can be elliptical in shape exhibiting different structure in different directions. The wind breaking through the holes in the inner dense shell can accelerate a layer at intermediate radii, and the inner nebular region may be a mixture of faster and slower matter. The outer shell can fragment into clumps.

A 3D photoionization modelling which can address such situations has been applied to NGC 3132 by Monteiro et al. (2000). Such modelling usually attempts to fit the observed image of a nebula. Monteiro et al. reached an important conclusion that different geometries can reproduce the same observational data. The low-resolution spectroscopic data can be well modelled by an ellipsoidal geometry, but by using additional data from [S II] line ratios and [O III] velocity profiles they deduce a Diabolo-shape geometry for NGC 3132. However, in their calculations they made several simplifications, among them the assumption of a linearly increasing velocity field. Such modelling appears promising but at present still suffers from the large number of free parameters involved, and from the prohibitive CPU time needed for fully self-consistent calculations; because of these limitations, spherical models still should be considered as valuable approximations.

We discuss briefly two possibilities which may affect the discussion of Wray 16-423 and SMP 5 (the turbulent M2-31 is a different story).

10.1 Elliptical nebulae

We first investigate whether the central velocity cusp of the 'W' could be an artifact of the assumption of spherical sym-

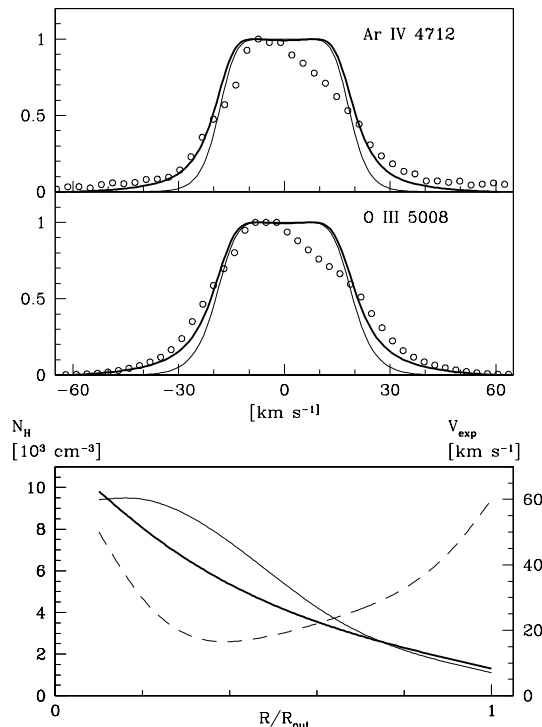


Figure 6. Two different density fields for Wray 16-423 resulting in different line shapes. Two upper panels present the emission line shapes for [O III] and [Ar IV] ions obtained with the same velocity field (dashed line in lower box) but with two density distributions (thin and thick lines in lower box).

metry. This is done for the case of Wray 16-423 where some evidence for ellipticity exists. The requirement for a high velocity region comes from the extended wings of the [O III] and [Ar IV] lines: we therefore attempt to reproduce these without such a region.

To approximate an elliptical model, we use a two-component model. This essentially doubles the number of free parameters, so that one can expect that the data can be fitted much more easily but the uniqueness of the model will be affected. To limit the number of free parameters, we fix the inner and outer radius, and the velocity profile, and only vary the density distribution. Compared to our spherical model, one of the components must be opaque with an ionization boundary at our estimated outer radius. This component will explain the observed low excitation lines. The second component has a lower density, giving a transparent model with the same outer radius. (A different outer radius could be assumed but this would be wholly unconstrained with the present data.)

We adopt a 'U'-shaped velocity field which is the same in all directions, as found observationally for NGC 7027 (Walsh et al. 1997a). Our question is now whether a density profile exists for the transparent component which can reproduce the line wings. One such possibility is presented in Fig. 6. This shows that a relatively small change in density distribution will shift the line formation zones of [O III] and [Ar IV] ions outwards so that the line wings trace the

outermost acceleration. The density should in fact not be too much lower, otherwise the line wings would be too weak to be observed. Not shown are the He II line which is also well fitted and other observed low excited lines which are not fitted.

This example suggests a possible explanation of our observations, not in terms of a variable velocity in the intermediate region, but a variable azimuthal ionization stratification with a simpler velocity field. This discussion certainly concerns also SMP 5. The turbulent velocity field of the third PN could not easily be fitted in this way.

It is well known (Gruenwald et al. 1997) that without spherical symmetry the outward-only approximation fails. This approximation is applied in our photoionization code. Therefore we refrain from quantitative analysis. The tentative model is only intended to give support for the considered possibility.

10.2 Clumps and irregularities

PNe show a wealth of sub and microstructures, including clumping. The best known case is perhaps the Helix, but HST shows small structures in many objects. However they are far easier seen in images than in spectra. High density clumps tend to have lower temperatures (e.g. the dusty Helix globules observed by Meaburn et al. (1992), low ionization knots seen in images of Balick (1987) and discussed by Kahn & Breitschwerdt 1990), while the forbidden lines are highly temperature sensitive and tend to trace the extended gas.

Large and bright knots are also observed in some nebulae. However, the case of NGC 6543 analyzed by Bryce et al. (1992) shows that the explosive appearance seen in images in fact corresponds to a relatively inert kinematic situation where the bright knots are co-moving with the faint halo. Also Corradi et al. (2000b) when analyzing nebulae IC 2553 and NGC 5882 found that knots visible in low-ionization lines do not show evidence of moving with peculiar velocities compared with the general motion.

However, clumps can affect the velocity structure. If the inner dense shell is clumpy, the fast wind from the central star could be breaking through the holes, and set up a secondary swept-up shell at a larger radius, in the lower density outer regions. Such an effect is seen in the Abell nebulae A30 and A78, which have dense clumps very close to the star, with a cometary appearance, and an irregular, accelerated shell at about 0.5 of the outer radius (Meaburn et al. 1998, Meaburn & López 1996). In these objects the location of the fast wind is obvious in observations, as it is hydrogen-poor.

It is also possible that the outer shell is clumpy, e.g., as in the already mentioned IC 2553 and NGC 5882. Both PNe reveal a double shell structure; both outer shells are more spherical and expand faster than the inner shells. The low ionization knots, of intriguing origin, follow the movement of the surrounding outer shells. This also gives a situation, as in the elliptical model above, where the same accelerated outer regions can explain both the extended wings of high excited lines in the transparent fragments, and the line splitting of the low excited lines in the opaque fragments.

11 CONCLUSIONS

High-resolution echelle observations, covering a range of emission lines, provide a powerful tool to study the velocity distribution inside (unresolved) planetary nebulae. We analyze three objects, in the Bulge, the Sagittarius Dwarf galaxy and the SMC. They show similar structure: a small inner radius, a dense inner region and a lower-density outer shell. The dynamical core masses are almost equal, around $0.62 M_{\odot}$, in spite of very different metallicities and progenitor masses. All three PNe show evidence for jumps in expansion velocity, at various locations in the nebulae. The velocity stratification as found in our spherical model is supported by the observed ion stratification. In Wray 16-423 and M 2-31 we detect different line splitting for different ions, confirming that the low excitation ions trace more extended regions.

The proximity of the dense inner shell to the central star is not seen in the existing hydrodynamical models. The assumptions concerning late AGB and early post-AGB mass-loss evolution need to be verified to model the three presented PNe.

Three main velocity features appear. Velocity maxima are found at the inner and the outer edge of the nebulae. The outer acceleration is a common, known feature; the evidence for the innermost acceleration is new. (In one case, M 2-31, the evidence at the inner edge is tentative as we lack a good probe for the region.) Hydrodynamic models, and energy arguments, strongly suggest that the inner one is due to acceleration by the fast wind from the hot central star. The outer one can be explained as the overpressured ionized region pushing into the outer AGB wind. The third feature is a high velocity, low density region affecting the intermediate excitations ions, which is seen in two objects. The origin of this region is not clear. Three possible explanations are given, all of which have some support in models and/or observations of PNe. First, it can be associated with a weak shock seen in hydrodynamical models at the boundary where the dense inner shell expands into the lower-density region. However, the observed feature is much stronger than in the model. Second, it can be due to an ellipticity of the nebula, where in a direction with lower density, the line formation region of the intermediate excitation ions extends into the outer acceleration zone. A similar situation could exist if the outer region is clumpy. Thirdly, the region could trace a secondary shell accelerated by a stellar wind breaking through an innermost clumpy region, as seen in, e.g., the PNe A30 and A78. It is not possible to decide on the correct explanation based on the present data.

One nebula shows evidence for either fine radial velocity structure, or strong turbulence. This PN has a [WC]-type central star, a characteristic which has previously been linked to turbulent nebulae. There are indications for an anti-correlation between density and velocity. We suggest that the apparent turbulence may be a superposition of many shocks with velocity near the sound speed. Such waves could perhaps be caused by a time-variable [WC]-wind.

ACKNOWLEDGMENTS

K. Gesicki acknowledges support from 'Polish State Committee for Scientific Research' grant No. 2.P03D.020.17. The

observer at the NTT was David Pinfield. The research was supported by grants from the British Council and by a PPARC Visitors Grant.

REFERENCES

- Acker A., Gesicki K., Grosdidier Y., Durand S., 2002, *A&A*, 384, 620
- Acker A., Köppen J., Stenholm B., Raytchev B., 1991, *A&AS*, 89, 237
- Balick B., 1987, *AJ* 94, 671
- Blöcker T., 1995, *A&A*, 299, 755
- Breitschwerdt D., Kahn F. D., 1990, *MNRAS* 244, 521
- Bryce M., Meaburn J., Walsh J. R., Clegg R. E. S., 1992, *MNRAS* 254, 477
- Corradi R.L.M., Schönberner D., Steffen M., Perinotto M., 2000a, *A&A*, 354, 1071
- Corradi R.L.M., Gonçalves D. R., Villaver E., Mampaso A., Perinotto M., 2000b, *ApJ* 542, 861
- Dolphin A.E., Walker A.R., Hodge P.W., Mateo M., Olszewski E.W., Schommer R.A., Suntzeff N.B., 2001, *ApJ*, 562, 303
- Dopita M.A., Henry J.P., Tuohy I.R., et al., 1990, *ApJ*, 365, 640
- Dudziak G., Péquignot D., Zijlstra A.A., Walsh J.R., 2000, *A&A*, 363, 717
- Gathier R., Pottash S.R., Goss W.M., van Gorkom J.H., 1983, *A&A*, 128, 325
- Gesicki K. & Acker A., 1996, *Ap&SS*, 238, 101
- Gesicki K. & Zijlstra, A. A., 2000, *A&A*, 358, 1058
- Gesicki K., Acker A., Szczerba R., 1996, *A&A*, 309, 907
- Gesicki K., Zijlstra A.A., Acker A., Szczerba R., 1998, *A&A*, 329, 265
- Górny S.K., 2001, in: *Low-Mass Wolf-Rayet Stars: Origin and Evolution*, *Ap&SS*, 275, 67
- Grosdidier Y., Acker A., Moffat A.F.J., 2000, *A&A*, 364, 597
- Gruenwald R., Viegas S. M., Brogiere D., 1997, *ApJ* 480, 283
- Harrington J.P., Borkowski K.J., Tsvetanov Z., 1995, *ApJ*, 439, 264
- Hashimoto O., 1994, *A&AS*, 107, 445
- Henry R.B.C., 1989, *MNRAS*, 241, 453
- Herwig F., Schönberner D., Blöcker T., 1998, *A&A*, 340, L43
- Kahn F.D., West K.A., 1985, *MNRAS*, 212, 837
- Leene A., Pottasch S.R., 1987, *A&A*, 173, 145
- Liu X.-W., Barlow M.J., Blades J.C., et al., 1995, *MNRAS*, 276, 167
- Marten H. & Szczerba R., 1997, *A&A*, 325, 1132
- Meaburn J., Walsh J. R., Clegg R. E. S., Walton N. A., Taylor D., Berry D. S., 1992, *MNRAS* 255, 177
- Meaburn J. & López J.A., 1996, *ApJ*, 472, L45
- Meaburn J., López J.A., Bryce M., Redman M.P., 1998, *A&A*, 334, 670
- Mellema G., 1994, *A&A*, 290, 915
- Mellema G., 1995, *MNRAS* 277, 173
- Mellema G., 1997, *A&A* 321, L29
- Mellema G., 2001, in: *Low-Mass Wolf-Rayet Stars: Origin and Evolution*, *Ap&SS*, 275, 147
- Monteiro H., Morisset C., Gruenwald R., Viegas S. M., 2000, *ApJ* 537, 853
- Neiner C., Acker A., Gesicki K., Szczerba R., 2000, *A&A*, 358, 321
- Parthasarathy M., Acker A., Stenholm B., 1998, *A&A*, 329, L9
- Pauldrach A., Puls J., Kudritzki R.P., Mendez R.H., Heap S.R., 1988, *A&A*, 207, 123
- Péquignot D., Walsh J.R., Zijlstra A.A., Dudziak G., 2000, *A&A*, 361, L1
- Perinotto M., Kifonidis K., Schönberner D., Marten H., 1998, *A&A*, 332, 1044
- Piatti A.E., Santos J.F.C., Claria J.J., Bica E., Sarajedini A., Geisler D., 2001, *MNRAS*, 325, 792
- Schmidt-Voigt M. & Köppen J., 1987, *A&A*, 174, 211
- Schönberner D. & Steffen M., 1999, in: *Optical and infrared spectroscopy of circumstellar matter* (Eds. E.W. Günther, B. Stecklum, S. Klose), *ASP Conf. Ser.*, Vol. 188, p. 281
- Soker N., 2002, *A&A* 386, 885
- Stasinska G., Richer M.G., McCall M.L., 1998, *A&A*, 336, 667
- Tylenda R., Acker A., Stenholm B., 1993, *A&AS*, 102, 595
- Van de Steene G.C. & Zijlstra, A.A., 1994, *A&AS*, 108, 485
- Van den Bergh S., 2000, *The Galaxies of the Local Group* (Cambridge University press)
- Vassiliadis E. & Wood P.R., 1993, *ApJ*, 413, 641
- Walsh J. R., Dudziak G., Walton N. A., 1997a, in: *IAU Symp. 180 "Planetary nebulae"*, Eds. H.J.Habing and H.J.G.L.M.Lamers (Kluwer, Dordrecht), p. 286
- Walsh J.R., Dudziak G., Minniti D., Zijlstra A.A., 1997b, *ApJ*, 487, 651
- Zijlstra A.A., Pottasch S.R., Bignell C., 1989, *A&AS*, 79, 329
- Zijlstra A.A., Walsh J.R., 1996, *A&A*, 312, L21
- Zijlstra A.A., Bedding T.R., Mattei J., 2002, *MNRAS*, in press